Tunable Superconducting Qubits with Flux-Independent Coherence

M. D. Hutchings,[1] J. B. Hertzberg,[2] Y. Liu,[1] N. T. Bronn,[2] G. A. Keefe,[2] Markus Brink,[2] Jerry M. Chow,[2] and B. L. T. Plourde[1]

[1]*Department of Physics, Syracuse University, Syracuse, New York 13244, USA*
[2]*IBM, T. J. Watson Research Center, Yorktown Heights, New York 10598, USA*

(Received 17 February 2017; revised manuscript received 17 May 2017; published 12 October 2017)

We study the impact of low-frequency magnetic flux noise upon superconducting transmon qubits with various levels of tunability. We find that qubits with weaker tunability exhibit dephasing that is less sensitive to flux noise. This insight is used to fabricate qubits where dephasing due to flux noise is suppressed below other dephasing sources, leading to flux-independent dephasing times $T_2^* \sim 15$ μs over a tunable range of approximately 340 MHz. Such tunable qubits have the potential to create high-fidelity, fault-tolerant qubit gates and to fundamentally improve scalability for a quantum processor.

DOI: 10.1103/PhysRevApplied.8.044003

I. INTRODUCTION

Quantum computers have the potential to outperform classical logic on important technological problems. A practical quantum processor must be composed of quantum bits ("qubits") that are isolated from environmental decoherence sources yet easily addressable during logical gate operations. Superconducting qubits are an attractive candidate because of their simple integration with fast control and readout circuitry. In recent years, advances in superconducting qubits have demonstrated how such integration may be achieved while maintaining high coherence [1–3]. Further extensions of qubit coherence will serve to reduce gate errors, cutting down on the number of qubits required for fault-tolerant quantum logic [4,5].

An important aspect of maintaining high qubit coherence is the reduction of dephasing. Frequency-tunable qubits are inherently sensitive to dephasing via noise in the tuning control channel. Tuning via a magnetic flux thus introduces dephasing via low-frequency flux noise [6–13]. Such noise is ubiquitous in thin-film superconducting devices at low temperatures. Experiments indicate a high density of unpaired spins on the thin-film surface [14], with fluctuations of these spins leading to low-frequency flux noise that typically has a $1/f$ power spectrum [13,15–17]. For any flux-tunable qubit, this flux noise leads to significant dephasing whenever the qubit is biased at a point with a large gradient of qubit energy with respect to flux.

Flux tuning is, nonetheless, highly advantageous for many quantum circuits, and several classes of quantum logic gates rely on flux-tunable qubits. In the controlled-phase gate [1,18], qubit pairs are rapidly tuned into resonance to create entanglement. Here, both flux noise and off-resonant coupling to other qubits produce phase errors proportional to gate times, with the total gate error scaling as the square of the gate time [19]. Alternatively, fixed-frequency qubits have been employed in schemes such as the cross-resonance (CR) gate [20,21] to demonstrate aspects of quantum error correction [3,22]. Recent efforts with two-qubit devices have extended CR gate fidelities beyond 99% [23]. Larger lattices of fixed-frequency qubits, however, are likely to suffer increasingly from frequency crowding. If a qubit's 0-1 excitation frequency overlaps with the 0-1 or 1-2 frequency of its neighbor, or if the two qubits' frequencies are very far apart, the CR gate between these two qubits will not be ideal, with a strong possibility of leakage out of the computational subspace, or a very weak gate, respectively [24]. However, fixed-frequency transmon qubits are challenging to fabricate to a precision better than about 200 MHz [25]. Given such imprecision, a hypothetical 17-qubit logic circuit could see up to a quarter of its gate pairs fail due to frequency crowding (see Appendix A). Frequency-tunable transmon qubits, therefore, appear to be attractive for use in architectures based on the CR gate.

In this paper, we show how a tunable qubit's sensitivity to flux noise may be reduced by limiting its extent of tunability. We report results for several different qubits, showing that the qubit dephasing rate is proportional to the sensitivity of the qubit frequency to magnetic flux and to the amplitude of low-frequency flux noise. Furthermore, we use the understanding gained through this study to fabricate a qubit whose dephasing due to non-flux-dependent sources exceeds its dephasing due to low-frequency flux noise over a range of more than 300 MHz of tunability. This unique qubit has the potential to reduce errors in gates employing frequency-tunable qubits and to evade frequency crowding in qubit lattices employing CR gates. It therefore offers a promising route for creating high-fidelity two-qubit gates that reach fault-tolerant gate operation and for improving the scalability of superconducting qubit devices.

Our device adapts a design in which a superconducting quantum-interference device (SQUID) serves as the Josephson inductance in a transmon qubit [26]. Here, the

 © 2017 American Physical Society

Josephson energy—and, consequently, the qubit 0-1 transition frequency f_{01}—may be tuned with a magnetic flux Φ with a period of $\Phi_0 \equiv h/2e$, the magnetic flux quantum, where h is Planck's constant and e is the electron charge. However, if the two junctions in the SQUID have the differing Josephson energies E_{J1} and E_{J2}, a so-called asymmetric transmon is formed [27]. The greater the difference in junction energies, the smaller the level of tunability. If $E_{J1} > E_{J2}$, we can define the ratio as $\alpha = E_{J1}/E_{J2}$, and the sum as $E_{J\Sigma} = E_{J1} + E_{J2}$. The total flux-dependent Josephson energy E_J varies according to the following expression from Ref. [26]:

$$E_J(\Phi) = E_{J\Sigma}\cos\left(\frac{\pi\Phi}{\Phi_0}\right)\sqrt{1 + d^2\tan^2\left(\frac{\pi\Phi}{\Phi_0}\right)}, \quad (1)$$

where d is given as $d = (\alpha - 1)/(1 + \alpha)$.

II. DEVICE DESIGN AND FABRICATION

Considering the expectation that qubits on a single chip should experience a common flux-noise level, we prepare two styles of sample, A and B, shown in Fig. 1. We vary α in sample A to observe the effect on dephasing and include fixed-frequency qubits in both samples as a reference for non-flux-dependent dephasing. Each chip includes eight separate cavity-qubit systems in a multiqubit planar circuit quantum electodynamics (cQED) architecture. Sample A includes transmon qubits of the design found in Refs. [3,22], with readout resonators frequency multiplexed and coupled to a common feed line for microwave drive and readout. Sample B employs the qubit design of Refs. [23,28,29], with a separate microwave port for each readout resonator. In sample B, coplanar-waveguide buses, resonant at approximately 6 GHz, couple the qubits together three at a time to form a lattice for multiqubit gate operations, as in Refs. [28,29], although no such operations are presented in this paper. In sample A, we adjust the junction areas to prepare transmons having the junction ratios $\alpha = 7$, 4, and 1. To keep $E_{J\Sigma}$ fixed among the qubits, we keep the total junction area fixed, while the single-junction qubit maintains the same SQUID loop structure, with one of the junctions left open. In sample B, we design six qubits to have $\alpha = 15$, while two employ a single junction matching the values of E_{J1} of the tunable qubits.

To fabricate both sample A and sample B, we use standard photolithography and plasma etching to pattern the coplanar waveguides, ground plane, and qubit capacitors from a sputtered Nb film on a Si substrate. In sample A, the Nb films are 100 nm thick. In sample B, they are 200 nm thick. Electron-beam lithography and conventional double-angle shadow evaporation is used to form Al-AlOx-Al tunnel junctions and the traces connecting them to the transmon shunt capacitors. In samples A and B, the differing separation between capacitor pads necessitates different SQUID loop geometries, as shown in Fig. 1. The effects of loop geometry on flux noise have been the subject of recent studies [30,31]. In sample A, the SQUID loops comprise 0.6-μm-wide Al traces bridging the 20-μm gap between the transmon capacitor pads, and we adjust the junction area by adjusting the junction width, keeping the overlap fixed at 0.2 μm. In sample B, SQUID loops have a 2-μm trace width and join with Nb leads extending from the capacitor pads, which have a 70-μm separation. In sample B, we adjust the junction sizes via both width and overlap. In both sample A and sample B, the SQUID loop area is approximately 400 μm^2.

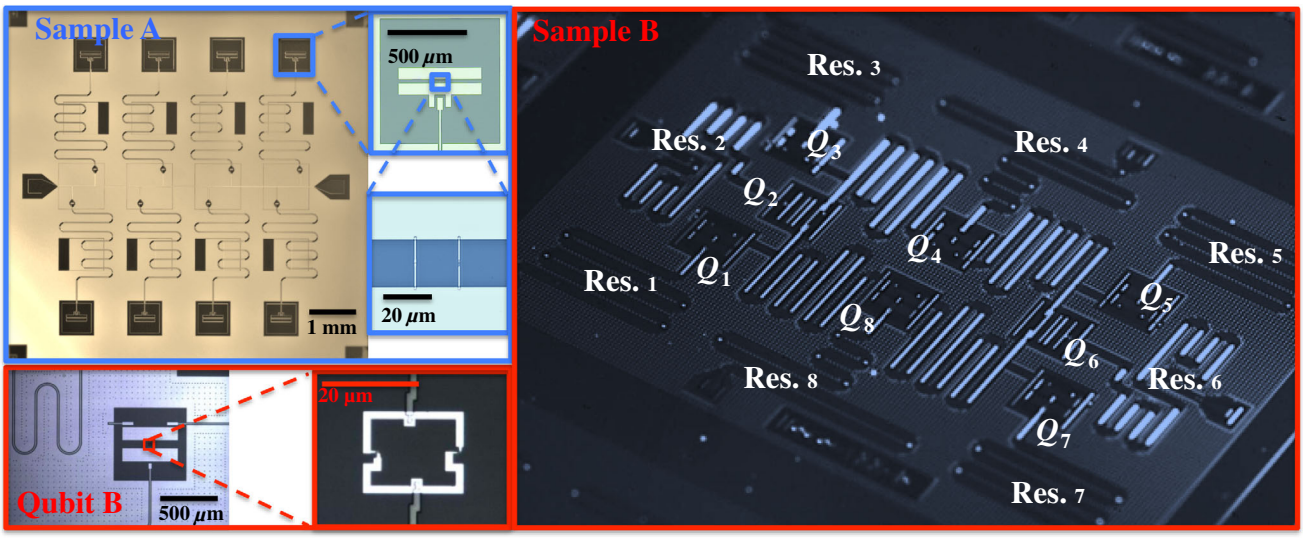

FIG. 1. Optical micrographs of samples including higher magnification images of qubits and SQUID loops. The sample-B image is a chip of identical design to the one used for our measurements. In the sample-B image, labels indicate each qubit and its individual readout resonators, while unlabeled resonators are bus resonators.

III. EXPERIMENT

Measurements of sample A are completed in a dilution refrigerator (DR) at Syracuse University, while sample B is measured in a DR at the IBM T. J. Watson Research Center. Samples are wire bonded onto holders designed to suppress microwave chip modes, mounted to the mixing chamber of the DR and placed inside a Cryoperm magnetic shield, thermally anchored at the mixing chamber. Both DRs incorporate room-temperature μ-metal shields.

For sample A, room-temperature microwave signals are supplied through attenuated coaxial lines, thermalized at each stage of the DR and filtered using 10-GHz low-pass filters (K&L) thermalized at the mixing chamber. We use a total of 70 dB of attenuation on the drivelines: 20 dB at 4 K, 20 dB at 0.7 K, and 30 dB at the mixing chamber, with a base temperature of 30 mK. Output measurement signals from the sample pass through another 10-GHz low-pass filter, a microwave switch, and two magnetically shielded cryogenic isolators, all thermally anchored to the mixing chamber. In the case of sample A, the signal is amplified by a low-noise HEMT at 4 K, passing through a Nb/Nb superconducting coaxial cable between the mixing chamber and the 4-K stage. The signal is amplified further at room temperature before being mixed down to 10 MHz and digitized. The eight resonators, coupled to each of their respective qubits in sample A, have measured frequencies that range from 6.975 to 7.136 GHz, separated by approximately 20–25 MHz. Linewidths $\kappa/2\pi$ for these resonators are on the order of a few hundred kilohertz.

Figure 1 shows the layout of the sample-B chip. The $\alpha = 15$ asymmetric SQUID transmon reported in this paper is located at position Q_7. It is read out through a coplanar-waveguide resonator of frequency 6.559 GHz and linewidth of about 300 kHz, and it is found to have $f_{01}^{\max} = 5.387$ GHz. The fixed-frequency transmon (5.346 GHz) at position Q_2 is read out through a 6.418-GHz resonator having a linewidth of approximately 300 kHz. Sample-B qubits are measured via signal wiring similar to that presented in Refs. [3,22,28,32]. Drive wiring includes 10 dB of attenuation at 50 K, 10 dB at 4 K, 6 dB at 0.7 K, and 10 dB at 100 mK, and, at the mixing-chamber plate, there is 30 dB of attenuation plus a homemade "Eccosorb" low-pass filter. Drive signals enter a microwave circulator at the mixing plate. On one set of signal wiring, the second port of the circulator passes directly to the readout resonator for qubit Q_7. In another set of signal wiring, the second port of the circulator passes to several different qubits via a microwave switch. Signals reflected from the device pass back through the circulator to the output and amplifier circuitry. Output circuitry comprises a low-pass Cu powder filter, followed by two cryogenic isolators in series, followed by an additional low-pass filter, followed by a superconducting NbTi coaxial cable, followed by a low-noise HEMT amplifier at 4 K and an additional low-noise amplifier at room temperature. Low-pass filters are intended to block signals above about 10 GHz. In the case of Q_7, additional amplification is afforded by a superconducting low-inductance undulatory galvanometer (SLUG) amplifier [33] mounted at the mixing stage, biased via two bias-tee networks and isolated from the sample by an additional cryogenic isolator. Output signals are mixed down to 5 MHz before being digitized and averaged. The mixing-plate thermometer indicates a temperature of about 15–20 mK during measurements.

Magnetic flux is supplied to sample A via an approximately 6-mm-inner-diameter superconducting wire coil placed 2 mm above the sample and fed via brass coaxial lines thermally anchored at each stage of the DR, with an 80-MHz π filter at 4 K and a copper powder filter on the mixing chamber. Sample B is flux biased using a wire-wound superconducting coil mounted about 3 mm above the qubit chip and fed via dc pair wiring (Cu above 4 K within the fridge, NbTi below). The coil has a self-inductance of 3.9 mH and a mutual inductance to the SQUID loop of approximately 1 pH. Coils are current biased using SRS SIM928 dc-voltage sources through a 2-kΩ or 5-kΩ room-temperature resistor. dc flux is applied simultaneously to all qubits on a chip. For each qubit, we measure f_{01} as a function of coil current and fit this value against Eq. (1) to enable scaling of Φ_0 and to subtract any offset flux, as well as to determine $f_{01}^{\max}$ and asymmetry d. We treat the sign of flux as arbitrary. We observe no evidence of Ohmic heating due to current biasing of the coils. Specifically, over the range of applied fluxes, we observe a negligible change in fridge temperature, no trend in the coherence of fixed-frequency qubits, and no trend in the tunable qubits that is consistent with heating. Our use of superconducting coils and cabling, and the thermal anchoring of cabling, is effective in this regard.

Coherence measurements for both samples are performed using standard cQED readout techniques [34]. The flux level is set prior to qubit measurement and held fixed during the measurement. Using an automated measurement algorithm, qubit frequency is determined using Ramsey-fringe fitting, after which π and $\pi/2$ pulses are optimized at this frequency, and coherence is then measured. T_2^* is measured at a frequency detuning that offers sufficient fringes for fitting. If the automated tuning routine fails to find the frequency or properly scale the π and $\pi/2$ pulses, this point is omitted from the data set. All coherence data are visually checked before fitting and inclusion in the data set.

IV. RESULTS AND DISCUSSION

From the eight qubits on each chip, we present data from four qubits in sample A and two qubits in sample B, one of each variation from each sample. Figure 2 shows the flux dependence of f_{01}, subtracting fixed flux offsets for each qubit. The $\alpha = 15$ qubit has the weakest tunability: 337 MHz. Following Eq. (1) and the expectation that $f_{01} \propto \sqrt{E_J}$ [26],

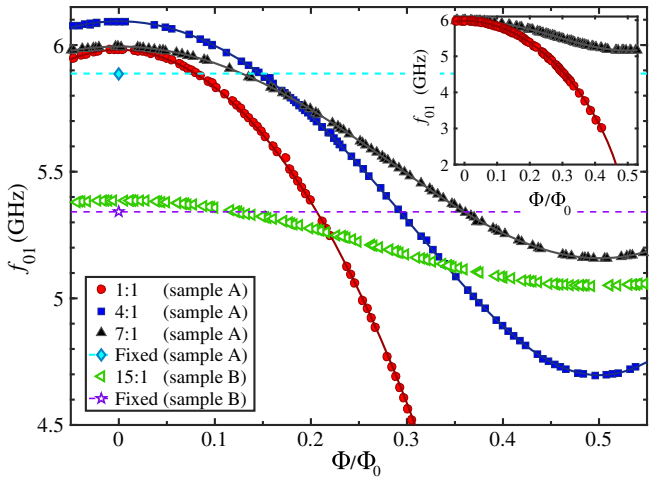

FIG. 2. f_{01} vs flux measured for qubits from samples A and B. Solid lines are fits to these tuning curves based on Eq. (1). Also included are frequencies of single-junction qubits from both samples. The dashed lines for these qubits serve as a guide for the eye. (Inset) The entire tuning range measured for the $\alpha = 1$ qubit, with the $\alpha = 7$ qubit included as a comparison to illustrate the large frequency tunability of an $\alpha = 1$ qubit.

we fit the data in Fig. 2 to find the maximum frequency $f_{01}^{\max} \propto \sqrt{E_{J\Sigma}}$ and the asymmetry parameter d. From the latter, we compute α and find that all of the qubits' measured asymmetry values are within 5% of the designed values. We note that the four sample-A qubits shown in Fig. 2 are designed to have identical values of $E_{J\Sigma}$—and therefore identical values of $f_{01}^{\max}$—but in fact exhibit an approximately 200-MHz spread, thus illustrating the challenge of fabricating qubits to precise frequencies.

To assess the effect of flux noise on dephasing, we observe how the latter relates to each qubit's frequency gradient as a function of flux $D_\Phi = |\partial f_{01}/\partial\Phi|$. We characterize dephasing via measurement of the Ramsey decay time T_2^*, which is sensitive to low-frequency dephasing noise [7,9]. We fit these Ramsey decay data using an exponential form. Although it has been shown that a dephasing noise source with a $1/f$ power spectrum will result in a Gaussian decay envelope [7,9], flux-independent dephasing sources such as cavity-photon shot noise [35–37] result in an exponential decay envelope. Ramsey decays for fixed-frequency qubits are, therefore, well fit with an exponential decay envelope. For all of our asymmetric transmons, as well as a large portion of the dephasing data for the $\alpha = 1$ symmetric device, we find that an exponential decay envelope is also a good fit. As detailed in Appendix D, we find systematic but slight differences between the values of T_2^* obtained using an exponential or Gaussian fit. Assuming a purely exponential decay sets an upper bound on the extracted flux-noise level.

Relaxation times T_1 range from about 20 to 50 μs over the six qubits reported here. In general, T_1 increases with decreasing qubit frequency (Appendix B, Fig. 5), consistent with dielectric loss and a frequency-independent loss tangent, as observed in other tunable superconducting qubits [38]. Qubits in sample A remain sufficiently detuned below their readout resonators to neglect Purcell relaxation, but the T_1 of the $\alpha = 15$ qubit in sample B exhibits frequency dependence consistent with Purcell losses. T_1 relaxation due to coupling to a flux-bias line, first discussed for inductive coupling in Ref. [26], and for capacitive coupling in Ref. [39], is considered for the qubits studied here. We show in Appendix C that flux-line coupling to our qubits sets an upper bound on T_1 not significantly lower than that reported in Ref. [26], and still orders of magnitude greater than current experimental T_1 times.

To compare dephasing rates among the qubits, we use the relation $\Gamma_\phi = 1/T_2^* - 1/2T_1$ [40] to remove the relaxation contribution. The resulting dephasing rate Γ_ϕ is plotted against flux in Fig. 3. As the curves in Fig. 2 illustrate, the integer and half-integer Φ/Φ_0 points are "sweet spots" where $D_\Phi = 0$, and thus the qubit is first-order insensitive to flux noise. All the transmons in sample A clearly exhibit a dephasing rate that increases with D_Φ and is at a minimum at the sweet spots. Second-order sensitivity to flux noise [9,41] should be negligible in our samples because of the small energy-band curvature. However, the level of Γ_ϕ for the nontunable qubit on each sample and the tunable qubits at their sweet spots indicates the presence of non-flux-dependent sources of dephasing. Such background dephasing may arise from other mechanisms, including cavity-photon shot noise [35], critical current noise [42], or charge noise affecting the residual charge dispersion in the transmon design [26]. This background dephasing may be expected to vary from qubit to qubit due to differences in qubit-cavity coupling or cavity

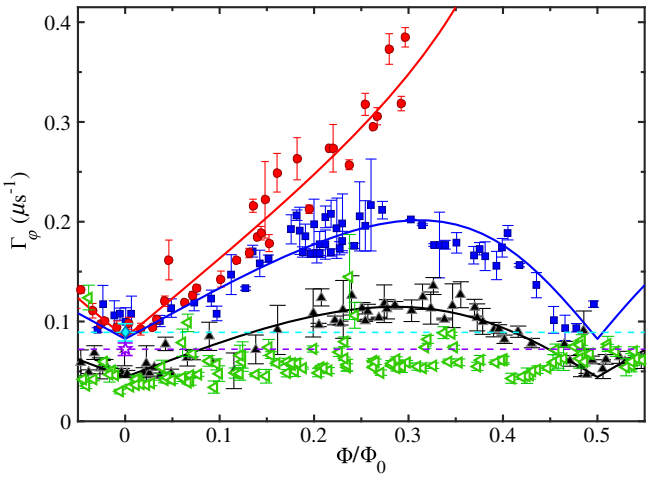

FIG. 3. Γ_ϕ vs flux measured for qubits from samples A and B. Solid lines show a simultaneous fit of the form $mD_\Phi + b$ to the tunable qubits in sample A. Factor m is common to all three data sets, while b is allowed to vary for each. Γ_ϕ, measured for fixed-frequency qubits in both samples, is included with dashed lines as a guide for the eye.

thermalization, among other effects. Such variations are commonly observed in multiqubit devices [3,22,28].

We note that the behavior of the other qubits on our chips, where it could be measured, is consistent with the six devices presented here. In sample A, the position of the flux coil on the sample holder enables only one each of the $\alpha = 4$ and $\alpha = 7$ transmons to be tuned through a full flux quantum; these data appear in the figures. The $\alpha = 1$ qubit not shown in the figures has an anomalously high background dephasing rate, making its flux-noise dephasing difficult to distinguish. The single-junction transmon not shown in the figures has the dephasing $\Gamma_\phi = 0.102\ \mu s^{-1}$. In sample B, we measure dephasing of three $\alpha = 15$ qubits and two single-junction qubits. None of the tunable qubits exhibit any flux dependence in its dephasing. The qubit of each type having the lowest dephasing rate is shown in the figures. The single-junction qubit not shown in the figures exhibits dephasing of $0.129\ \mu s^{-1}$, while the mean dephasing rates of the tunable qubits not shown in the figures are 0.110 and $0.144\ \mu s^{-1}$.

For sample A, if we consider only flux-dependent dephasing, it is evident that $\Gamma_\phi \propto D_\Phi$. Furthermore, qubits of the same geometry on the same chip should experience similar flux noise [14]. The analysis outlined in Refs. [7,9] may then be used to extract a flux-noise level from the relationship between Γ_ϕ and D_Φ. We apply a simultaneous fit of the form $mD_\Phi + b$ to the $\alpha = 1$, 4, and 7 qubits, allowing background dephasing b to vary for each qubit, while a single m is common to all. The fit appears as solid lines in Fig. 3. We derive $\Gamma_\phi = 2\pi\sqrt{A_\Phi |\ln(2\pi f_{IR} t)|} D_\Phi$ following the approach in Ref. [9], where the flux-noise power spectrum is $S_\Phi(f) = A_\Phi/|f|$, f_{IR} is the infrared cutoff frequency, taken to be 1 Hz, and t is on the order of $1/\Gamma_\phi$, which we take to be $10\ \mu s$ in our calculations. Equating mD_Φ to Γ_ϕ in the equation above, we may calculate the flux-noise level in sample A. To determine the uncertainty in the measured flux-noise level, we must not only account for the error in fitting m but also how variations in dephasing time impact the calculation of A_Φ values. To account for the latter, we determine the impact on extracted $A_\Phi^{1/2}$ as t is varied. Adjusting t over a range similar to what we observe experimentally leads to an approximately 10% change in $A_\Phi^{1/2}$. The errors we report for all calculated $A_\Phi^{1/2}$ values reflect this added uncertainty. The choice of $f_{IR} = 1$ Hz is related to the typical measurement time for a Ramsey decay. Variations in the value for this cutoff frequency have only a weak impact on the extracted value of $A_\Phi^{1/2}$. We find that $A_\Phi^{1/2} = 1.4 \pm 0.2\ \mu\Phi_0$ in sample A. This level is compatible with previous experimental studies of flux noise in superconducting flux [6–8,43,44] and phase qubits [45].

To achieve an even clearer picture of the influence of flux noise on these qubits, we plot Γ_ϕ vs D_Φ for each qubit in Fig. 4(a). Here, D_Φ is computed from the fits to the energy

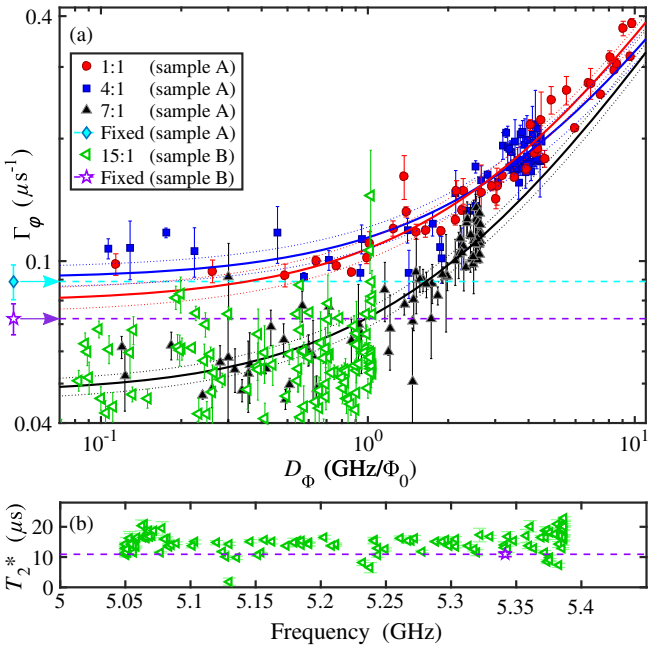

FIG. 4. (a) Γ_ϕ vs D_Φ measured for qubits from samples A and B. Solid lines show individual linear fits to the tunable qubits in sample A, as described in the text. Note that the scale is log log. Γ_ϕ, measured for fixed-frequency qubits in both samples, is included with dashed lines as a guide for the eye. (b) T_2^* vs frequency measured for the $\alpha = 15$ and fixed-frequency qubits in sample B.

bands of each qubit shown in Fig. 2. This plot exhibits a linear dependence where the slope can be related to the amplitude of the flux noise and the offset corresponds to the background dephasing level. In this case, instead of a simultaneous fit, we apply a separate fit of $\Gamma_\phi = mD_\Phi + b$ to each qubit, and we find $A_\Phi^{1/2}$ values of 1.3 ± 0.2, 1.2 ± 0.2, and $1.4 \pm 0.2\ \mu\Phi_0$ for the $\alpha = 7$, 4 and 1 qubits, respectively. These flux-noise levels are all consistent with past studies of low-frequency flux noise in superconducting devices [6–8,43–45].

In Fig. 4(a), it can be seen that, for the tunable qubits in sample A, within the range $D_\Phi \lesssim 1\ \mathrm{GHz}/\Phi_0$, the measured dephasing rate is largely flux independent within the experimental spread. To exploit this insensitivity, we design the tunable transmon in sample B to have a D_Φ no greater than approximately $1\ \mathrm{GHz}/\Phi_0$ at any point within its tuning range, a condition satisfied by having $\alpha = 15$. As a result, its sensitivity to $1/f$ flux noise appears to be suppressed below the level where background dephasing dominates. Γ_ϕ is essentially flat across the entire tuning range, as shown in Fig. 3, with a mean of $0.058\ \mu s^{-1}$ and experimental scatter of $\sigma \sim 0.017\ \mu s^{-1}$. By comparison, this sample's fixed-frequency qubit exhibits $\Gamma_\phi = 0.072\,\mu s^{-1}$. Figure 4(b) shows clearly that T_2^* for the $\alpha = 15$ qubit in sample B is independent of frequency over the whole tuning range.

Although no significant flux dependence of the dephasing is detectable for sample B, we estimate from our earlier expression for Γ_ϕ that the observed scatter is consistent with $A_\Phi^{1/2}$ of 0.9 $\mu\Phi_0$. Recent progress in understanding the origins of $1/f$ flux noise in SQUIDs [46] has facilitated up to a $5\times$ reduction in A_Φ [47]. Such reductions applied to the sample B qubit would reduce its maximum flux-noise-driven dephasing below 0.008 μs^{-1}. In an $\alpha = 7$ qubit tunable over more than 700 MHz, flux noise of such a level would cause dephasing no greater than 0.017 μs^{-1}. Alternatively, in a qubit with 150-MHz tunability, the flux noise seen in sample B would cause dephasing not exceeding 0.008 μs^{-1}, or only 0.004 μs^{-1} if the flux noise were reduced as in Ref. [47]. We may contrast these values with the non-flux-noise-driven dephasing seen in state-of-the-art single-junction transmons used for multiqubit gate operations: $\Gamma_\phi = 0.004$ to 0.008 μs^{-1} on two-qubit samples [23,32], 0.01 μs^{-1} on five-qubit samples [29], and 0.01 to 0.021 μs^{-1} on seven-qubit samples [28]. We also note that the two SQUID designs A and B (Fig. 1) exhibit no difference in flux-noise level within experimental uncertainties.

V. CONCLUSIONS

In this paper, we show that, by reducing the flux tunability of a transmon qubit, we can dramatically lower its sensitivity to $1/f$ flux noise. Using this understanding, we fabricate a qubit in which the dephasing rate due to flux noise is suppressed below the level set by non-flux-dependent sources. This device exhibits a flux-independent dephasing rate $\Gamma_\phi \sim 0.06$ μs^{-1} over a tunable range in excess of 300 MHz.

As qubit architectures progress in complexity, frequency crowding and flux-noise dephasing will present increasing challenges to gate fidelity. A recently demonstrated quantum computing prototype employed nine individually-flux-tuned superconducting qubits [2]. The qubit design shown in this paper should be readily adaptable to this and other types of existing multiqubit architectures using either frequency-tuned gates or all-microwave gates. In order to avoid Ohmic heating in larger architectures, the flux tuning must employ strictly superconducting wiring and may benefit from persistent-current operation at set points [48]. Notwithstanding such engineering issues, the qubit design presented here offers a scalable means to avoid both frequency crowding and flux-noise dephasing in multiqubit gates, thus addressing a key challenge in realizing a logically encoded qubit and a fault-tolerant universal quantum computer.

ACKNOWLEDGMENTS

We acknowledge support from Intelligence Advanced Research Projects Activity (IARPA) under Contract No. W911NF-16-0114. The device fabrication was performed in part at the Cornell NanoScale Facility, a member of the National Nanotechnology Coordinated Infrastructure (NNCI), which is supported by the National Science Foundation under Grant No. ECCS-1542081. We thank Y.-K.-K. Fung, J. Rohrs, and J. R. Rozen for their experimental contributions, and R. McDermott and T. Thorbeck for providing the SLUG amplifier and assistance with its setup. We also thank J. M. Gambetta, E. Magesan, R. McDermott, D. C. McKay, and S. Rosenblatt for the helpful discussions.

APPENDIX A: NONIDEAL FABRICATION IN FIXED-FREQUENCY QUBITS

Lattices of coupled qubits are proposed to enable error-correction algorithms such as the "surface code" [4,5]. Qubits are arranged into a square grid with alternate qubits serving either data or error-checking functions. Bus couplers provide interaction among adjacent qubits, with up to four qubits attached to each bus. A seven-qubit lattice thereby comprises 12 qubit pairs, and a 17-qubit lattice comprises 34 pairs. However, when fabricating single-junction transmon qubits, it is challenging to achieve a frequency precision of $\sigma_f < 200$ MHz [25]. Such imprecision will inhibit functioning of qubit lattices. Considering a lattice of transmon qubits with a frequency of about 5 GHz and an anharmonicity $\delta/2\pi = -340$ MHz, and considering cross-resonance gate operations, we can estimate the number of undesired interactions among these pairs. Studies of the cross-resonance gate [24] indicate that these gates will be dominated by undesirable interactions if the frequency separation $|\Delta|$ between adjacent qubits is equal to zero (degeneracy between f_{01} of the qubits), or is equal to $-\delta/2\pi$ (degeneracy between f_{01} of one qubit and f_{12} of the next), or if $|\Delta| > -\delta/2\pi$ (weak interaction leading to very slow gate operation). In a simple Monte Carlo model, we assign to all points in the lattice a random qubit frequency from a Gaussian distribution centered on 5 GHz, and we count the number of degenerate or weak-interaction pairs, taking a range of $\pm(\delta/2\pi)/20$, or ± 17 MHz around each degeneracy. The results appearing in Table I make it evident that the likelihood of frequency collisions increases as the lattice grows.

TABLE I. Frequency-collision modeling in lattices of transmon qubits employing cross-resonance gates. The predicted number of bad gate pairs ('frequency collisions') in two different lattice sizes. A 7-qubit lattice has 12 pairs, and a 17-qubit lattice has 34 pairs. The mean of distribution is 5 GHz, and two different distribution widths σ_f are considered.

Number of qubits	σ_f	Mean number of collisions
7	$\frac{1}{2}\lvert\delta/2\pi\rvert$	2.3
7	$\frac{3}{4}\lvert\delta/2\pi\rvert$	3.6
17	$\frac{1}{2}\lvert\delta/2\pi\rvert$	6.6
17	$\frac{3}{4}\lvert\delta/2\pi\rvert$	10.6

APPENDIX B: QUBIT COHERENCE

For sample A, three T_1 measurements are made at each flux point, followed by three T_2^* measurements. At each flux point, the reported T_1 and T_2^* values and error bars comprise the mean and standard deviations of the three measurements. The corresponding Γ_ϕ value is found from these mean values, and its error bar is found by propagating the errors in T_1 and T_2^* through a partial derivative and combining these errors in a quadrature sum. For sample B, at each flux point, T_1 is measured first, then T_2^*, three times in succession. For this device, the reported T_1 and T_2^* values comprise the mean of the three measurements, and the error bars are their standard deviation. Here, the reported dephasing rate Γ_ϕ comprises the mean $\langle 1/T_2^* - 1/2T_1 \rangle$ found with the three T_1, T_2^* pairs, and the error bar is the standard deviation. The uncertainties of the individual fits are significantly smaller than the standard deviation among several measurements, suggesting a time variation in both T_1 and T_2^*.

Figure 5 shows T_1 plotted versus qubit frequency, measured for the qubits discussed in our paper. We observe a trend of an increasing T_1 with a decreasing qubit frequency. In sample A, each qubit's quality factor ωT_1 is roughly constant, consistent with dielectric loss and a frequency-independent loss tangent, as observed in other tunable superconducting qubits [38]. In sample B, T_1 decreases by about 10 μs from the low to the high end of the frequency range, consistent with the Purcell loss to the readout resonator. In addition, fine structure is occasionally observed in Fig. 5, where T_1 drops sharply at specific frequencies. These localized features in the T_1 frequency dependence are observed for all tunable qubits that we have measured. These features, similar to those observed in Ref. [38], are attributed to frequencies where a qubit transition is resonant with a two-level system defect on or near the qubit. Additionally, in sample B, at a few

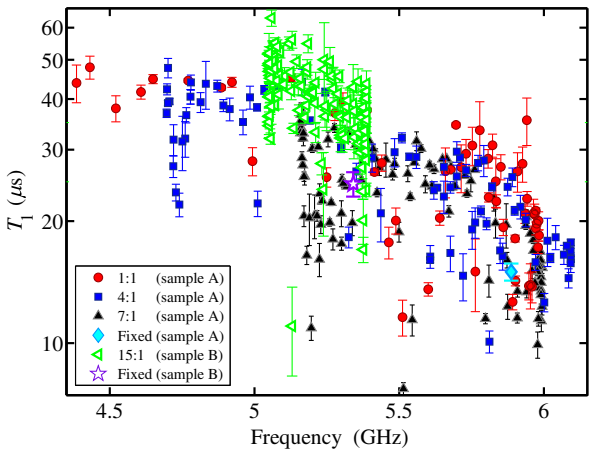

FIG. 5. T_1 vs frequency measured for all qubits discussed in the main text. Single points included for T_1 values measured for the fixed-frequency qubits.

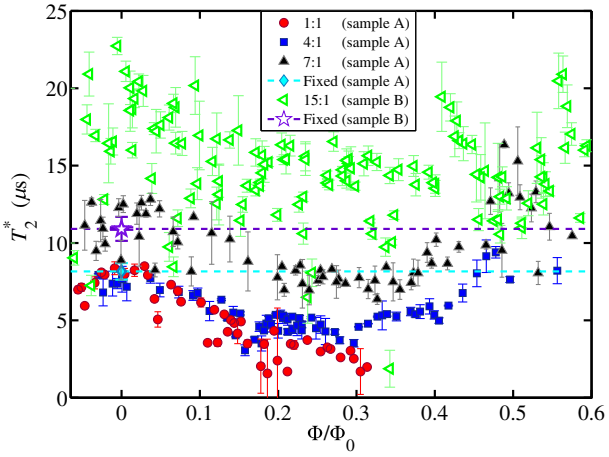

FIG. 6. T_2^* vs flux measured for the qubits discussed in the main text. The T_2^* values measured for the fixed-frequency qubits in both samples are included with dashed lines as a guide for the eye.

frequency points, interqubit coupling affects relaxation. When qubit Q_7 is tuned to be nearly degenerate with the fixed-frequency qubit Q_6 (at approximately 5.33 GHz) or to an adjacent tunable qubit Q_8 (at about 5.22 GHz), coupling via the adjacent buses produces an avoided crossing in the energy spectrum. This effect is barely noticeable in either the frequency curve of Fig. 2 or the relaxation data in Fig. 5.

Figure 6 shows T_2^* plotted versus flux, measured for the qubits discussed in our paper. For the tunable qubits in sample A, T_2^* is greatest at the qubit sweet spots and decreases away from these sweet spots as D_Φ increases. In the $\alpha = 15$ tunable qubit (Q_7) in sample B, T_2^* is nearly constant over the measured half-flux-quantum range. The small frequency dependence observed in T_2^* in sample B is consistent with the observed variation of T_1 with frequency, leading to the frequency-independent dephasing rate observed for this qubit in Fig. 3.

APPENDIX C: RELAXATION DUE TO COUPLING TO FLUX-BIAS LINE

Using a dc SQUID for the inductive element of a transmon allows for frequency tuning via magnetic flux, but it opens up a channel for energy relaxation into the dissipative environment across the bias coil, via the mutual inductance M. Koch *et al.* showed in Eq. (2.17) of Ref. [26] that the Josephson portion of the qubit Hamiltonian can be written in terms of a phase variable with a shifted minimum that depends upon the qubit's asymmetry and the applied flux bias. By linearizing this Hamiltonian for small noise amplitudes near the static flux-bias point, the authors compute the relaxation rate for a given current noise power related to the impedance R across the flux-bias coil and the mutual inductance between the coil and the SQUID loop.

Their analysis was presented for the case of a transmon containing a near-symmetrical SQUID. Here, we apply their analysis to cases of increasing junction asymmetry, assuming harmonic-oscillator wave functions for the qubit's ground and excited states.

Using our typical device parameters ($E_J/h = 20$ GHz, $E_c/h = 350$ MHz, $M = 2$ pH, $R = 50\ \Omega$), we obtain the resulting dependence of T_1 as a function of bias flux, shown in Fig. 7 for the asymmetries discussed in our paper. For a 10% junction asymmetry, this contribution results in a T_1 that varies between 25 ms and a few seconds, in agreement with Ref. [26]. As the junction asymmetry is increased, the minimum T_1 value, obtained at odd half-integer multiples of Φ_0, decreases, but, even for our $\alpha = 15$ qubit, the resulting T_1 value never falls below 10 ms, 2 orders of magnitude larger than the measured T_1 value due to all other mechanisms in current state-of-the-art superconducting qubits.

In Ref. [26], Koch *et al.* also describe a second loss channel for a transmon related to coupling to the flux-bias line. In this case, the relaxation occurs due to the oscillatory current through the inductive element of the qubit—independent of the presence of a SQUID loop—coupling to the flux-bias line, described by an effective mutual inductance M'. This mutual inductance vanishes when the Josephson element of the qubit and the bias line are arranged symmetrically. With a moderate coupling asymmetry for an on-chip bias line, Koch *et al.* estimate that the T_1 corresponding to this loss mechanism would be on the order of 70 ms [26]. Because this mechanism does not directly involve the presence of a SQUID loop, this particular limit on T_1 should be no different for an asymmetric SQUID transmon than for a conventional transmon. An additional potential relaxation channel may arise due to capacitive coupling to the flux-bias line, as discussed in Ref. [39]. However, this coupling is expected to be negligible where a remote wire-wound field coil is used, as in our experiments.

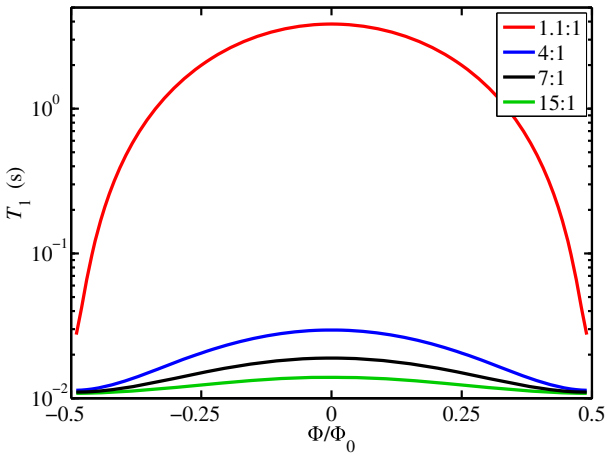

FIG. 7. Dependence of T_1 with flux for asymmetric transmons, calculated for the asymmetries discussed in the main text, due to coupling to an external flux bias following the analysis of Koch *et al.* [26]. Although, in our experiments, the symmetric qubit has the value $\alpha = 1$, in this calculation, $\alpha = 1.1$ is used so that T_1 does not diverge at $\Phi = 0$.

APPENDIX D: RAMSEY DECAY FITTING

As described in Sec. IV, our analysis of qubit dephasing rates uses a purely exponential fit to all of the measured Ramsey decays. Here, we discuss why this fitting approach is appropriate for all asymmetric qubits and a large portion of the coherence data measured for the symmetric qubit.

Of all the qubits measured in this study, the symmetric $\alpha = 1$ qubit is most affected by flux noise away from the qubit sweet spot because of its large energy-band gradient. Therefore, to illustrate the impact that flux noise has upon the Ramsey decay envelope, we consider the Ramsey measurements for this qubit on and off the sweet spot. Example measurements are shown at flux values of 0 and 0.3 Φ_0 in Figs. 8(a) and 8(b), respectively. At each flux point, we fit the Ramsey decay with both a purely exponential [Fig. 8(a)(I)] and a purely Gaussian form [Fig. 8(a)(II)]. The residuals of each fit are included to compare the quality of fit in each case. As discussed in the main text, at the upper sweet spot, where $D_\Phi = 0$, non-flux-dependent background dephasing should dominate and the Ramsey decay should be more readily fit using an exponential. Figure 8(a) shows that this is indeed the case: the purely exponential fit provides a more precise fit to the Ramsey decay, with the residuals to this fit being smaller over the entire range compared to those corresponding to the Gaussian fit. The Ramsey decay shown in Fig. 8(b) is measured at a point where D_Φ is the maximum measured for the $\alpha = 1$ qubit. Here, it is clear that a purely Gaussian form results in a better fit with smaller residuals than an exponential envelope. This finding indicates that, at this flux point, the $\alpha = 1$ qubit is heavily impacted by low-frequency flux noise, as a purely $1/f$ dephasing source would result in a Gaussian envelope for the decay [9]. Although a purely Gaussian fit form is useful for illustrating the impact that flux noise has upon the Ramsey decay form, it is not the optimal quantitative approach for investigating dephasing in these qubits. This is because tunable transmons dephase not only due to flux noise with a roughly $1/f$ power spectrum, but also due to other noise sources with different non-$1/f$ power spectra [35–37]. These other noise sources generally result in an exponential dephasing envelope. Also, a Ramsey decay has an intrinsic loss component that is always exponential in nature. Therefore, to accurately fit decay due to dephasing in these qubits, we must account for these exponential decay envelopes in any fitting approach that is not purely exponential.

To account for the T_1 contribution to the Ramsey decay envelope in our nonexponential fitting, we take the average

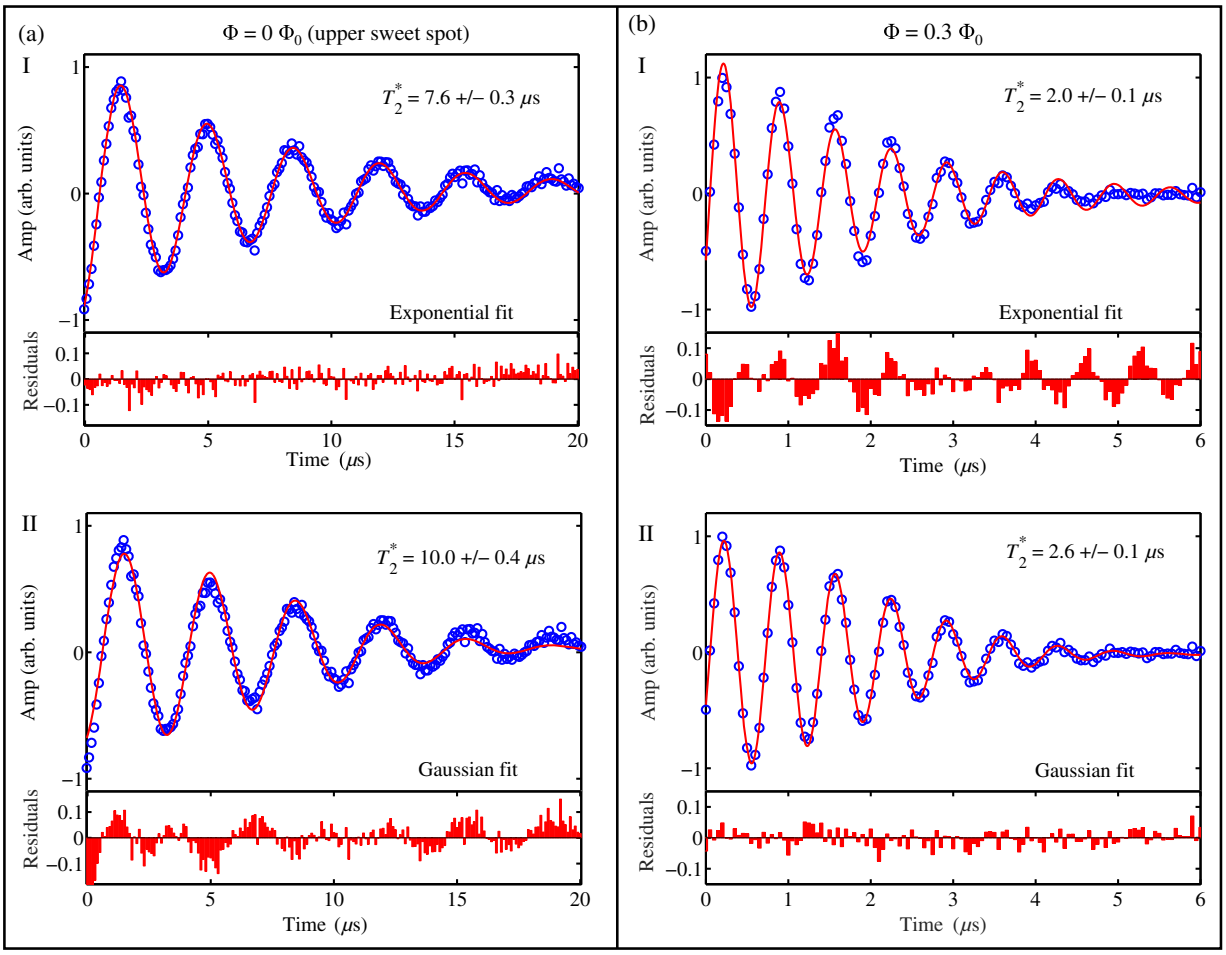

FIG. 8. Ramsey decay envelopes measured for the $\alpha = 1$ qubit at (a) the sweet spot $\Phi = 0$ and (b) $\Phi = 0.3\Phi_0$, where D_Φ is the largest value measured for this qubit. At each flux point, the Ramsey decay envelopes are fit with both (I) a purely exponential and (II) a Gaussian fit form. Functions fitted to the measured data (the blue open circles) plotted as solid red lines.

T_1 measured at each flux point and separate it from T_2^* in the Ramsey fit function using $1/T_2^* = 1/T_\phi + 1/2T_1$. Therefore, instead of fitting a T_2^* time, we fit T_ϕ directly. To fit the Ramsey decay using a Gaussian fit form, we square the dephasing exponent within the fitting function [Eq. (D1)]. We can go one step further by not forcing an explicit fit form to the dephasing exponent, but instead adding another fit parameter γ [Eq. (D2)], which would be 1 for a pure exponential fit and 2 for a pure Gaussian one. Although a fit that is not explicitly exponential or Gaussian is not motivated directly by a particular theoretical model, by fitting Ramsey decays with this free exponent γ, we gain insight into the transition from flux-noise-dominated dephasing at large D_Φ to background dephasing near the sweet spots. The two separate fit forms described above are given by the following decay functions:

$$f_{\text{Ramsey}}(t) = A + B\{\cos(\omega t + \delta)\exp(-\Gamma_1 t/2) \times \exp[-(\Gamma_\phi t)^2]\}, \quad \text{(D1)}$$

$$f_{\text{Ramsey}}(t) = A + B\{\cos(\omega t + \delta)\exp(-\Gamma_1 t/2) \times \exp[-(\Gamma_\phi t)^\gamma]\}, \quad \text{(D2)}$$

where A and B are magnitude and offset constants to adjust the arbitrary measured signal, ω is the detuning of the Ramsey pulses from the qubit frequency with a phase offset δ, Γ_1 is the intrinsic loss rate $(1/T_1)$, and Γ_ϕ is the dephasing rate. Here, A, B, ω, δ, Γ_ϕ, and γ are the fit parameters. All other components are fixed with values determined using the methods discussed above.

This behavior is illustrated in Fig. 9, where we plot γ vs flux extracted from fits to the Ramsey measurements on the $\alpha = 1$ qubit using Eq. (D1). In the flux region between $+/-0.1\Phi_0$, $\gamma \approx 1$, indicating that the dephasing envelope is primarily exponential, and thus that the dominant dephasing noise affecting the qubits here does not have a $1/f$ spectrum. At flux-bias points farther away from the sweet spot, γ shifts towards 2 as D_Φ increases and appears to level off close to this value at flux biases above

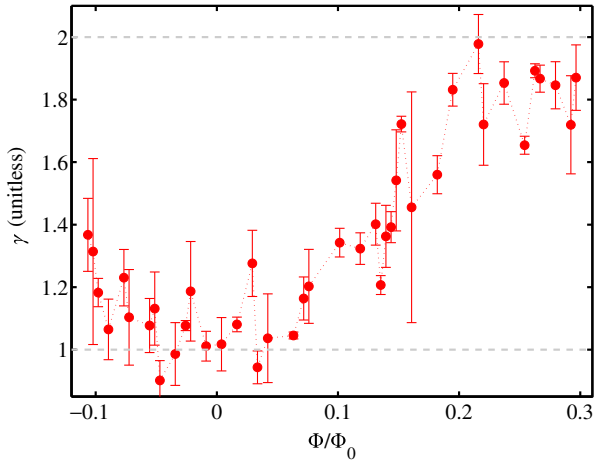

FIG. 9. γ vs flux extracted from fits to the Ramsey measurements on the $\alpha = 1$ qubit using Eq. (D2).

approximately $0.2\Phi_0$. Thus, in this bias regime, the dephasing envelope is primarily Gaussian and the dephasing noise influencing the qubits is predominantly low frequency in nature with a $1/f$-like spectrum [7,9].

We can also visualize this variable-exponent fit by plotting γ vs D_Φ rather than Φ, again, for the $\alpha = 1$ qubit (Fig. 10). In this plot, γ approaches 2 for D_Φ values of around 6 GHz/Φ_0. We also include vertical dashed lines in Fig. 10 indicating the maximum D_Φ values reached by the less tunable $\alpha = 4$ and 7 qubits in sample A. Below these D_Φ levels, γ is close to 1, implying that the decay envelope is nearly exponential, and thus justifying our use of an exponential decay for fitting the asymmetrical qubits in the main text.

As yet-another approach to fitting the Ramsey decay envelopes, we can employ a function that separates the

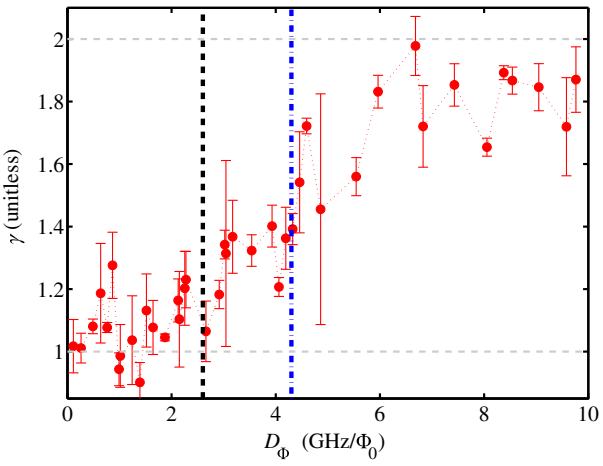

FIG. 10. γ vs D_Φ extracted from fits to the Ramsey measurements on the $\alpha = 1$ qubit using Eq. (D2). The dashed lines are included to indicate the maximum D_Φ value reached by the $\alpha = 7$ (black dashed line) and $\alpha = 4$ (blue dotted-dashed line) qubits measured in sample A.

exponential dependence from background dephasing from the Gaussian form due to dephasing from noise with a low-frequency tail. For this fit, along with separating out the T_1 contribution to the Ramsey decay envelope, we also determine the non-flux-dependent background dephasing rate at the sweet spot, then use this rate as a fixed parameter in the fitting of our Ramsey measurements at any given flux point. We now have a composite Ramsey fit form that has three components: a T_1 contribution and a background dephasing component that are purely exponential and fixed by the fitting of separate measurements, plus a Gaussian component to capture the dephasing due to noise with a $1/f$ spectrum. This analysis leads to a composite fitting function of the form:

$$f_{\text{Ramsey}}(t) = A + B\{\cos(\omega t + \delta)\exp(-\Gamma_1 t/2) \times \exp(-\Gamma_{\phi,\text{bkg}} t)\exp[-(\Gamma_\phi t)^2]\}, \tag{D3}$$

where A and B are magnitude and offset constants to adjust the arbitrary measured signal, ω is the detuning from the qubit frequency with a phase offset δ, Γ_1 is the intrinsic loss rate $(1/T_1)$, $\Gamma_{\phi,\text{bkg}}$ is the background dephasing rate measured at $D_\Phi = 0$ and Γ_ϕ is the fitted dephasing rate. Here, A, B, ω, δ, and Γ_ϕ are the fit parameters. All other components are fixed with values determined using the methods discussed above. Although this fit form separates the different components to dephasing decay well, it has one key deficiency: it assumes that the background dephasing rate is frequency independent, which is not necessarily justified, as the background dephasing mechanism may also vary with frequency. To calculate the total dephasing rate using this fit form, we add the constant background dephasing to the fitted Γ_ϕ value.

To understand how the explicit fitting form impacts the dephasing rate, in Fig. 11, we plot the Γ_ϕ vs D_Φ calculated for the $\alpha = 1$ qubit using four different fitting forms: exponential, Gaussian [Eq. (D1)], γ exponent [Eq. (D2)], and composite [Eq. (D3)]. We first note that any differences in the rate of dephasing calculated at each point using the various fit methods are subtle and that the fits are reasonably consistent with one another within the fit error bars and scatter. We do observe, though, that a purely exponential fit results in a dephasing rate that is slightly higher than the values from the Guassian fits for all flux points, resulting in the largest slope and thus the highest effective flux-noise level. Therefore, we conclude that forcing a purely exponential fit to the Ramsey decay envelopes measured for qubits that are strongly influenced by $1/f$ flux noise simply puts an upper bound on the absolute flux-noise strength. The γ-exponent fitting approach provides a dephasing rate that agrees well with that extracted from the exponential fit form at low D_Φ values where background dephasing processes dominate. However, at higher D_Φ values where the qubit is heavily

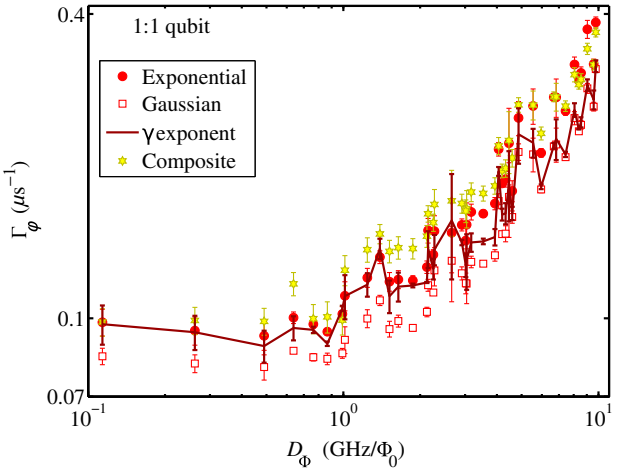

FIG. 11. Γ_ϕ vs D_Φ calculated for the $\alpha = 1$ qubit using the exponential, Gaussian [Eq. (D1)], γ-exponent [Eq. (D2)], and composite [Eq. (D3)] fitting forms.

impacted by $1/f$ flux noise, the γ-exponent fit provides better agreement with the Gaussian-fitted dephasing rate.

The composite fit is rigidly fixed in the Γ_ϕ axis by the value chosen to match the background dephasing rate, in this case, chosen to match the rate observed at the lowest D_Φ value for the pure exponential fit. For this reason, direct comparisons at individual flux points between this fit and the others are more difficult. Despite all of these potential issues, the slope of Γ_ϕ vs D_Φ is independent of the chosen background dephasing rate. Therefore, this composite fit can be used to calculate a flux-noise level for this $\alpha = 1$ qubit, which takes into account both the exponential nature of non-flux-dependent dephasing and the Gaussian nature of $1/f$ flux-noise decay. Using the same methods outlined above, where we specify $\Gamma_\phi = 2\pi\sqrt{A_\Phi|\ln(2\pi f_{\mathrm{IR}} t)|}D_\Phi$, following the approach described in Ref. [9], we use the slope of this composite fit to extract a $1/f$ flux-noise level of $A_\Phi^{1/2} = 1.3 \pm 0.2\ \mu\Phi_0$. This approximately 10% reduction in the extracted flux-noise level for the $\alpha = 1$ qubit compared to the purely exponential fit ($A_\Phi^{1/2} = 1.4 \pm 0.2\ \mu\Phi_0$) brings it closer to the flux-noise level extracted from the fits to the measurements on the $\alpha = 7$ and 4 qubits: $1.3 \pm 0.2\ \mu\Phi_0$ and $1.2 \pm 0.2\ \mu\Phi_0$, respectively. The Ramsey measurements for these qubits are fit using a purely exponential fit form. It is important to note, though, that the approximately 10% reduction in the composite-fit-extracted flux-noise level for the $\alpha = 1$ qubit is within the error range associated with our flux-noise calculations.

We may summarize the results of this fitting study:

(1) The $\alpha = 1$ qubit in this study has a Ramsey decay envelope that is more Gaussian in nature at high D_Φ values, where the dephasing of this qubit is strongly influenced by low-frequency flux noise.

(2) Although we discuss different fitting approaches that better model the Ramsey decay envelope of qubits influenced by $1/f$ flux noise, using a purely exponential decay form for the Ramsey decay simply puts an upper bound on the extracted flux-noise strength. Also, the value of the flux-noise level and the dephasing rates are comparable to those we obtain with the various other fitting approaches.

(3) Using a Ramsey fit function that takes into account both the exponential nature of the T_1 contribution to the decay envelope and non-flux-dependent dephasing, as well as the Gaussian nature of dephasing due to $1/f$ flux noise, allows us to calculate a flux-noise level for the $\alpha = 1$ qubit that agrees well with the other, asymmetric qubits on the same sample. This agreement is expected, as qubits of the same geometry on the same chip should experience similar flux noise [14].

[1] R. Barends *et al.*, Superconducting quantum circuits at the surface code threshold for fault tolerance, Nature (London) **508**, 500 (2014).

[2] J. Kelly *et al.*, State preservation by repetitive error detection in a superconducting quantum circuit, Nature (London) **519**, 66 (2015).

[3] A. D. Córcoles, E. Magesan, S. J. Srinivasan, A. W. Cross, M. Steffen, J. M. Gambetta, and J. M. Chow, Demonstration of a quantum error detection code using a square lattice of four superconducting qubits, Nat. Commun. **6**, 6979 (2015).

[4] J. M. Gambetta, J. M. Chow, and M. Steffen, Building logical qubits in a superconducting quantum computing system, npj Quantum Inf. **3**, 2 (2017).

[5] A. G. Fowler, M. Mariantoni, J. M. Martinis, and A. N. Cleland, Surface codes: Towards practical large-scale quantum computation, Phys. Rev. A **86**, 032324 (2012).

[6] S. M. Anton, C. Müller, J. S. Birenbaum, S. R. OKelley, A. D. Fefferman, D. S. Golubev, G. C. Hilton, H. M. Cho, K. D. Irwin, F. C. Wellstood, G. Schön, A. Shnirman, and J. Clarke, Pure dephasing in flux qubits due to flux noise with spectral density scaling as $1/f^\alpha$, Phys. Rev. B **85**, 224505 (2012).

[7] F. Yoshihara, K. Harrabi, A. O. Niskanen, Y. Nakamura, and J. S. Tsai, Decoherence of Flux Qubits due to $1/f$ Flux Noise, Phys. Rev. Lett. **97**, 167001 (2006).

[8] J. Bylander, S. Gustavsson, F. Yan, F. Yoshihara, K. Harrabi, G. Fitch, D. G. Cory, Y. Nakamura, J. S. Tsai, and W. D. Oliver, Noise spectroscopy through dynamical decoupling with a superconducting flux qubit, Nat. Phys. **7**, 565 (2011).

[9] G. Ithier, E. Collin, P. Joyez, P. J. Meeson, D. Vion, D. Esteve, F. Chiarello, A. Shnirman, Y. Makhlin, J. Schriefl, and G. Schon, Decoherence in a superconducting quantum bit circuit, Phys. Rev. B **72**, 134519 (2005).

[10] E. Paladino, Y. M. Galperin, G. Falci, and B. L. Altshuler, $1/f$ noise: Implications for solid-state quantum information, Rev. Mod. Phys. **86**, 361 (2014).

[11] J. M. Martinis, S. Nam, J. Aumentado, K. M. Lang, and C. Urbina, Decoherence of a superconducting qubit due to bias noise, Phys. Rev. B **67**, 094510 (2003).

[12] F. C. Wellstood, C. Urbina, and J. Clarke, Low-frequency noise in dc superconducting quantum interference devices below 1 K, Appl. Phys. Lett. **50**, 772 (1987).
[13] C. M. Quintana *et al.*, Observation of Classical-Quantum Crossover of $1/f$ Flux Noise and Its Paramagnetic Temperature Dependence, Phys. Rev. Lett. **118**, 057702 (2017).
[14] S. Sendelbach, D. Hover, A. Kittel, M. Mück, J. M. Martinis, and R. McDermott, Magnetism in SQUIDs at Millikelvin Temperatures, Phys. Rev. Lett. **100**, 227006 (2008).
[15] L. Faoro and L. B. Ioffe, Microscopic Origin of Low-Frequency Flux Noise in Josephson Circuits, Phys. Rev. Lett. **100**, 227005 (2008).
[16] H. Wang, C. Shi, J. Hu, S. Han, C. C. Yu, and R. Q. Wu, Candidate Source of Flux Noise in SQUIDs: Adsorbed Oxygen Molecules, Phys. Rev. Lett. **115**, 077002 (2015).
[17] S. LaForest and R. de Sousa, Flux-vector model of spin noise in superconducting circuits: Electron versus nuclear spins and role of phase transition, Phys. Rev. B **92**, 054502 (2015).
[18] L. DiCarlo, J. M. Chow, J. M. Gambetta, L. S. Bishop, B. R. Johnson, D. I. Schuster, J. Majer, A. Blais, L. Frunzio, S. M. Girvin, and R. J. Schoelkopf, Demonstration of two-qubit algorithms with a superconducting quantum processor, Nature (London) **460**, 240 (2009).
[19] J. M. Martinis and M. R. Geller, Fast adiabatic qubit gates using only σ_z control, Phys. Rev. A **90**, 022307 (2014).
[20] C. Rigetti and M. Devoret, Fully microwave-tunable universal gates in superconducting qubits with linear couplings and fixed transition frequencies, Phys. Rev. B **81**, 134507 (2010).
[21] J. M. Chow, A. D. Córcoles, J. M. Gambetta, C. Rigetti, B. R. Johnson, J. A. Smolin, J. R. Rozen, G. A. Keefe, M. B. Rothwell, M. B. Ketchen, and M. Steffen, Simple All-Microwave Entangling Gate for Fixed-Frequency Superconducting Qubits, Phys. Rev. Lett. **107**, 080502 (2011).
[22] J. M. Chow, J. M. Gambetta, E. Magesan, D. W. Abraham, A. W. Cross, B. R. Johnson, N. A. Masluk, C. A. Ryan, J. A. Smolin, S. J. Srinivasan, and M. Steffen, Implementing a strand of a scalable fault-tolerant quantum computing fabric, Nat. Commun. **5**, 4015 (2014).
[23] S. Sheldon, E. Magesan, J. M. Chow, and J. M. Gambetta, Procedure for systematically tuning up cross-talk in the cross-resonance gate, Phys. Rev. A **93**, 060302 (2016).
[24] J. M. Gambetta, in *Lecture Notes of the 44th IFF Spring School*, edited by D. DiVincenzo (Forschungszentrum Jülich GmbH, Jülich, 2013).
[25] S. Rosenblatt, J. Hertzberg, M. Brink, J. Chow, J. Gambetta, Z. Leng, A. Houck, J. Nelson, B. Plourde, X. Wu, R. Lake, J. Shainline, D. Pappas, U. Patel, and R. McDermott, Variability metrics in Josephson Junction fabrication for Quantum Computing circuits, in *Proceedings of the APS March Meeting, New Orleans* (2017).
[26] J. Koch, T. M. Yu, J. Gambetta, A. A. Houck, D. I. Schuster, J. Majer, A. Blais, M. H. Devoret, S. M. Girvin, and R. J. Schoelkopf, Charge-insensitive qubit design derived from the Cooper pair box, Phys. Rev. A **76**, 042319 (2007).
[27] J. D. Strand, M. Ware, F. Beaudoin, T. A. Ohki, B. R. Johnson, A. Blais, and B. L. T. Plourde, First-order sideband transitions with flux-driven asymmetric transmon qubits, Phys. Rev. B **87**, 220505 (2013).
[28] M. Takita, A. D. Córcoles, E. Magesan, B. Abdo, M. Brink, A. Cross, J. M. Chow, and J. M. Gambetta, Demonstration of Weight-Four Parity Measurements in the Surface Code Architecture, Phys. Rev. Lett. **117**, 210505 (2016).
[29] IBM Quantum Experience, http://www.research.ibm.com/quantum/ (2017).
[30] S. M. Anton, J. S. Birenbaum, S. R. O'Kelley, V. Bolkhovsky, D. A. Braje, G. Fitch, M. Neeley, G. C. Hilton, H.-M. Cho, K. D. Irwin, F. C. Wellstood, W. D. Oliver, A. Shnirman, and J. Clarke, Magnetic Flux Noise in dc Squids: Temperature and Geometry Dependence, Phys. Rev. Lett. **110**, 147002 (2013).
[31] R. McDermott (private communication).
[32] S. Sheldon, L. S. Bishop, E. Magesan, S. Filipp, J. M. Chow, and J. M. Gambetta, Characterizing errors on qubit operations via iterative randomized benchmarking, Phys. Rev. A **93**, 012301 (2016).
[33] D. Hover, S. Zhu, T. Thorbeck, G. J. Ribeill, D. Sank, J. Kelly, R. Barends, J. M. Martinis, and R. McDermott, High fidelity qubit readout with the superconducting low-inductance undulatory galvanometer microwave amplifier, Appl. Phys. Lett. **104**, 152601 (2014).
[34] M. D. Reed, L. DiCarlo, B. R. Johnson, L. Sun, D. I. Schuster, L. Frunzio, and R. J. Schoelkopf, High-Fidelity Readout in Circuit Quantum Electrodynamics Using the Jaynes-Cummings Nonlinearity, Phys. Rev. Lett. **105**, 173601 (2010).
[35] A. P. Sears, A. Petrenko, G. Catelani, L. Sun, H. Paik, G. Kirchmair, L. Frunzio, L. I. Glazman, S. M. Girvin, and R. J. Schoelkopf, Photon shot noise dephasing in the strong-dispersive limit of circuit QED, Phys. Rev. B **86**, 180504 (2012).
[36] D. I. Schuster, A. Wallraff, A. Blais, L. Frunzio, R. S. Huang, J. Majer, S. M. Girvin, and R. J. Schoelkopf, ac Stark Shift and Dephasing of a Superconducting Qubit Strongly Coupled to a Cavity Field, Phys. Rev. Lett. **94**, 123602 (2005).
[37] J. Gambetta, A. Blais, D. I. Schuster, A. Wallraff, L. Frunzio, J. Majer, M. H. Devoret, S. M. Girvin, and R. J. Schoelkopf, Qubit-photon interactions in a cavity measurement-induced dephasing and number splitting, Phys. Rev. A **74**, 042318 (2006).
[38] R. Barends, J. Kelly, A. Megrant, D. Sank, E. Jeffrey, Y. Chen, Y. Yin, B. Chiaro, J. Mutus, C. Neill, P. O'Malley, P. Roushan, J. Wenner, T. C. White, A. N. Cleland, and J. M. Martinis, Coherent Josephson Qubit Suitable for Scalable Quantum Integrated Circuits, Phys. Rev. Lett. **111**, 080502 (2013).
[39] B. R. Johnson, Ph.D. thesis, Yale University, 2011.
[40] Y. Makhlin, G. Schön, and A. Shnirman, Quantum-state engineering with Josephson-junction devices, Rev. Mod. Phys. **73**, 357 (2001).
[41] Y. Makhlin and A. Shnirman, Dephasing of Solid-State Qubits at Optimal Points, Phys. Rev. Lett. **92**, 178301 (2004).
[42] D. J. Van Harlingen, T. L. Robertson, B. L. T. Plourde, P. A. Reichardt, T. A. Crane, and J. Clarke, Decoherence in

Josephson-junction qubits due to critical-current fluctuations, Phys. Rev. B **70**, 064517 (2004).

[43] J.-L. Orgiazzi, C. Deng, D. Layden, R. Marchildon, F. Kitapli, F. Shen, M. Bal, F. R. Ong, and A. Lupascu, Flux qubits in a planar circuit quantum electrodynamics architecture: Quantum control and decoherence, Phys. Rev. B **93**, 104518 (2016).

[44] M. Stern, G. Catelani, Y. Kubo, C. Grezes, A. Bienfait, D. Vion, D. Esteve, and P. Bertet, Flux Qubits with Long Coherence Times for Hybrid Quantum Circuits, Phys. Rev. Lett. **113**, 123601 (2014).

[45] R. C. Bialczak, R. McDermott, M. Ansmann, M. Hofheinz, N. Katz, E. Lucero, M. Neeley, A. D. O'Connell, H. Wang, A. N. Cleland, and J. M. Martinis, $1/f$ Flux Noise in Josephson Phase Qubits, Phys. Rev. Lett. **99**, 187006 (2007).

[46] S. Sendelbach, D. Hover, M. Mück, and R. McDermott, Complex Inductance, Excess Noise, and Surface Magnetism in dc SQUIDs, Phys. Rev. Lett. **103**, 117001 (2009).

[47] P. Kumar, S. Sendelbach, M. A. Beck, J. W. Freeland, Z. Wang, H. Wang, C. C. Yu, R. Q. Wu, D. P. Pappas, and R. McDermott, Origin and Reduction of $1/f$ Magnetic Flux Noise in Superconducting Devices, Phys. Rev. Applied **6**, 041001 (2016).

[48] G. Keefe, R. Koch, F. Milliken, and J. Rozen, Persistent current switch, U.S. Patent No. 8138880 B2 (20 March 2012).